Coverage Analysis of Remote Sensing Satellites in Concurrent Design Facility

Sergio Marín-Coca[1]; Elena Roibás-Millán[2]; and Santiago Pindado[3]

Abstract: This paper presents a new, accurate, and fast methodology, remote sensing satellites coverage analysis (RSS-CA) for determining the coverage area of Earth observation satellites in concurrent design facilities (CDFs) devoted to space mission analysis. The Earth observation areas of interest are discretized by grid points and the coverage surface is computed from the intersection between the grid and the satellite viewing geometry. This geometry is modeled for off-nadir pointing conical and rectangular field-of-view (FOV) sensors and considering a perfectly spherical Earth. To test the RSS-CA methodology, the MARTINLARA mission analysis was selected as a case study. This mission analysis was carried out at the CDF of the Instituto de Microgravedad "Ignacio Da Riva" (IDR/UPM Institute). The results were compared to the ones obtained with the well-known AGI System Tool Kit (STK) software. The high accuracy of the results shows that the developed methodology (RSS-CA) can be simply and effectively applied in CDFs designed for space mission analysis, representing the possibility of a more open and user-friendly environment in relation to other commercial tools. **DOI: 10.1061/(ASCE)AS.1943-5525.0001397.** © *2022 American Society of Civil Engineers.*

Introduction

In the early design of a space mission, exchanging ideas and data among experts of different engineering disciplines (also called subsystems) is essential. Almost all disciplines (e.g., structures, communications, power) have interactions with the others, so even small changes in a particular subsystem can involve the redesign of the whole space system. The traditional design methodology, including the one used in the aerospace industry, is the sequential approach. In such methodology, the overall design passes successively from one engineering domain specialist to another. It is an iterative process in which, sometimes, a miscommunication among the specialists can occur. Additionally, inconsistencies and incorrect assumptions may exist during the design process because the main design parameters are not updated in real time (Fortescue et al. 2011). Such problems can lead to a nonoptimal design, the decision-making process and the redesign phase being therefore prolonged.

A modern substitute to the sequential approach is concurrent engineering (CE). This methodology is based on applying techniques and processes that allow carrying out, by real-time teamwork, the product development activities (McDonald and Badescu 2014). A formal definition of CE adopted by the European Space Agency (ESA) is as follows: "Concurrent Engineering is a systematic approach to integrated product development that emphasises the response to customer expectations. It embodies team values of cooperation, trust and sharing in such a manner that decision making is by consensus, involving all perspectives in parallel, from the beginning of the product life-cycle" (Bandecchi et al. 2000). The space industry implemented CE in the 1980s, but it was first applied to a space mission at the Jet Propulsion Laboratory (JPL) in 1995, motivated by the National Aeronautics and Space Administration's (NASA's) faster, better, cheaper philosophy (Hihn et al. 2011).

The concurrent engineering design approach is mainly carried out within concurrent design facilities (CDFs). A CDF is a collaborative environment where the specialists of the different space disciplines work simultaneously and in coordination to perform conceptual and preliminary design of space missions. The main benefits derived from using a CDF are (1) the improvement of the quality of the design (more robust and optimized), (2) fast design iterations, and (3) the accumulation of corporate knowledge for further reusability. CDF users can work remotely with appropriate concurrent engineering tools (McDonald and Badescu 2014).

ESA began conducting pre-Phase A studies at its CDF located at the European Space Research and Technology Centre (ESTEC) in 1998 (Fortescue et al. 2011). Since then, ESA has performed around 250 studies and reviews of space missions, as shown in Fig. 1.

The implementation of the CDF has led to substantial improvement of the performance of the studies carried out by ESA, reducing time and costs, and has inspired the European space industry to create new CDFs for its own specific designs. Additionally, several universities have developed their own CDFs to support space mission studies and enhance the knowledge and expertise of its students on this matter. This is the case of the Instituto de Microgravedad "Ignacio Da Riva" (IDR/UPM Institute) at Universidad Politécnica de Madrid (UPM), which developed its CDF in 2011; since then, both academic work and real space projects have been conducted by using the CE tools developed for this facility (Roibás-Millán et al. 2018a, b; Bermejo et al. 2018; García-Pérez 2020) (Fig. 2).

The CDF of the IDR/UPM Institute is provided with both externally and internally developed software to design spacecraft

[1]Ph.D. Student, Universidad Politécnica de Madrid, Escuela Técnica Superior de Ingeniería Aeronáutica y del Espacio, Plaza del Cardenal Cisneros 3, 28040 Madrid, Spain; Ph.D. Student, Instituto Universitario de Microgravedad "Ignacio Da Riva" (IDR/UPM), Escuela Técnica Superior de Ingeniería Aeronáutica y del Espacio, Plaza del Cardenal Cisneros 3, 28040 Madrid, Spain (corresponding author). ORCID: https://orcid.org/0000-0003-0737-0613. Email: sergio.marin.coca@upm.es

[2]Professor, Instituto Universitario de Microgravedad "Ignacio Da Riva" (IDR/UPM), Escuela Técnica Superior de Ingeniería Aeronáutica y del Espacio, Universidad Politécnica de Madrid, Plaza del Cardenal Cisneros 3, 28040 Madrid, Spain. ORCID: https://orcid.org/0000-0003-0180-6973. Email: elena.roibas@upm.es

[3]Professor, Instituto Universitario de Microgravedad "Ignacio Da Riva" (IDR/UPM), Escuela Técnica Superior de Ingeniería Aeronáutica y del Espacio, Universidad Politécnica de Madrid, Plaza del Cardenal Cisneros 3, 28040 Madrid, Spain. ORCID: https://orcid.org/0000-0003-2073-8275. Email: santiago.pindado@upm.es

Note. This manuscript was submitted on July 28, 2021; approved on November 17, 2021; published online on January 20, 2022. Discussion period open until June 20, 2022; separate discussions must be submitted for individual papers. This paper is part of the ***Journal of Aerospace Engineering***, © ASCE, ISSN 0893-1321.

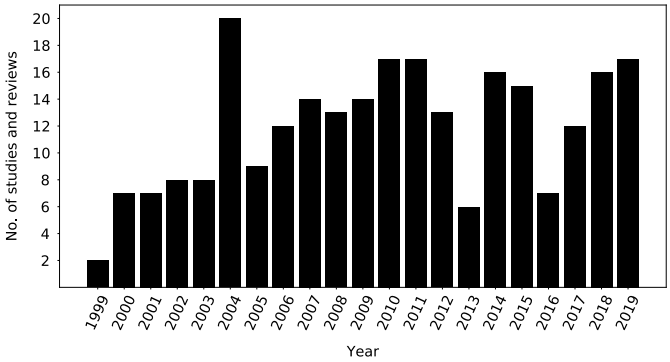

Fig. 1. Studies and reviews carried out by the ESA CDF by year. (Data from European Space Agency 2021.)

Fig. 2. CDF of the IDR/UPM Institute.

subsystems, support mission analysis, and manage costs and risks. The main reason to develop specific mission design software tools internally at IDR/UPM is the need for fast and simple calculations during the first phases of the spacecraft mission design because they are essential to perform trade-off studies and define some early mission solutions. Additionally, although commercial tools [e.g., General Mission Analysis Tool (GMAT), System Tool Kit (STK)] may produce accurate solutions, they are at the expense of large computing times and reduced user friendliness.

Furthermore, the success of projects carried out at the CDF of the IDR/UPM Institute is a consequence of many years of expertise in the field of aerospace engineering (Pindado et al. 2016). To give a clear example, the UPMSat-2 project has brought many research lines to the IDR/UPM Institute. These research lines include the following:

- Attitude Determination and Control Subsystems (ADCSs): The work of the IDR/UPM researchers has been driven toward control subsystems based on interaction with the Earth's magnetic field (Cubas et al. 2015a; Rodriguez-Rojo et al. 2019; Porras-Hermoso et al. 2021).
- Thermal control subsystems: Mainly based on ESATAN analysis (Gómez-San-Juan et al. 2018; Torralbo et al. 2018; Fernández-Rico et al. 2016; Gómez-San-Juan et al. 2020).
- Structural analysis of spacecraft and space instruments/systems (García-Pérez et al. 2018, 2019a, b, c).
- Spacecraft power subsystem devoted to photovoltaic systems (solar cells/panels) performance, harness design, and Li-ion batteries (Cubas et al. 2013; Pindado et al. 2018a; Roibás-Millán et al. 2020a, b; Cubas et al. 2014b, a, c, 2015b; Pindado et al. 2015; Pindado and Cubas 2017; Roibás-Millán et al. 2017; Cubas et al. 2017; Pindado et al. 2018b).

Aim of the Present Work

In 2019, a consortium of seven research groups of the Community of Madrid, Spain (IDR/UPM Institute and Desarrollo e Investigación Electromagnética (DIEMAG) from UPM; Radiofrequency, Electromagnetism, Microwaves and Antennas Group (GREMA), Plasma & Space Propulsion Team (EP2), and Optoelectronic and Laser Technology Group (GOTL) from Universidad Carlos III de Madrid; GEOSIGN from the National Geographic Institute of Spain; and Research Group on Space Astronomy and Data Mining (AEGORA) from Universidad Complutense de Madrid), one laboratory [National Institute for Aerospace Technology (INTA), Spain], one associated group [Instituto Astrofísico de Canarias (IAC), Spain], and two aerospace companies (AIRBUS DS and SENER) started the MARTINLARA project.

The goals of the MARTINLARA project are the development of a low-Earth orbit (LEO) nanosatellite and airborne validation of several technologies (IDR/UPM Institute 2020). Among these technologies, three microwave radiometers take measurements of the Earth's temperature and observe the interaction between the interplanetary dust and the Earth's magnetic field. Because the interaction is accentuated near the magnetic poles, high inclination orbits are good candidates for covering these areas. The IDR/UPM Institute carried out on its CDF a preliminary mission analysis to perform a study and subsequent trade-off analysis to select the best option between different orbits. The results were obtained with both GMAT and Analytical Graphics, Inc. (AGI) STK. Finally, the coverage statistics of the magnetic poles were calculated.

Subsequently, an advanced mission orbit analysis was performed by using the aforementioned software, being validated with the method described in this paper. This new methodology, called remote sensing satellites coverage analysis (RSS-CA), is a new procedure to the best of the authors' knowledge and is based on the available literature. Over several decades, several satellite coverage analysis methods have been published. These research works are focused on the determination of the visibility periods of ground targets by satellites. Conventional methods are based on establishing some geometrical conditions of visibility between satellites and targets and computing at all propagation time steps if these conditions are met (Escobal 1963; Wertz and Larson 1999; Ulybyshev 2000; Vallado 2013; Li et al. 2016; Crisp et al. 2018; Nugnes et al. 2019). These methods are precise but require a large computation effort if multiple satellites and targets are analyzed or the simulation lasts long. On the other hand, some other research works focused on developing fast algorithms to predict the visibility periods of satellites and targets (Salvatore et al. 1992; Ali et al. 1999; Mai and Palmer 2001; Cui and Han 2011; Sun et al. 2012; Han et al. 2017, 2018, 2019; Wang et al. 2019). To the authors' best knowledge, the study of the geometry of the instantaneous viewing areas seems to be only addressed in Nugnes et al. (2019). The methodology described in this paper, despite being very precise, only includes the study of conical sensors and requires many steps with a complex mathematical formulation. In order to overcome these limitations, the RSS-CA method described in this paper was developed at the IDR/UPM Institute, and it has been successfully implemented in the CDF of the IDR/UPM Institute to perform preliminary analysis of the coverage of satellites with remote sensing capabilities.

Remote sensing is a technique for detecting, monitoring, acquiring, processing, and analyzing the physical, chemical, and

biological characteristics (Liang et al. 2012) of an area from a distance. All objects emit, absorb, and reflect electromagnetic radiation that is characterized by its wavelength. Because every object has a unique spectral fingerprint, scientists use this knowledge to analyze the emitted and reflected radiation of the studied areas and to identify studied areas features (Campbell and Wynne 2011).

Artificial satellites that carry remote sensing instruments acquire large data sets with high resolution and precision for land, ocean, and atmosphere. These satellites have a frequency of data acquisition between once per minute and once per month, and their sensors operate in the visible, infrared, and microwave bands with spatial resolution ranging from centimeter scale to kilometer scale (Fu et al. 2019). Sensors aboard satellites are classified as passive and active. Passive sensors [e.g., digital cameras and infrared spectrometers (Toth and Jozkow 2016)] detect the emitted infrared radiation or the reflected sun radiation of the objects. On the other hand, active sensors [e.g., synthetic aperture radar (SAR) and lidar (Toth and Jozkow 2016)] emit electromagnetic radiation to the studied area and detect the reflected radiation.

The analysis of the coverage area of remote sensing satellites is necessary during its preliminary design phases. This allows selection between feasible orbits and payloads, and scheduling the operations of the satellite. Within this process, several variables are studied, such as the number of accesses to the target areas over a specific period, the fraction of the observed area, or the time elapsed between consecutive accesses (also known as revisit time).

As mentioned previously, the present paper describes a simple and fast methodology (RSS-CA) developed to carry out mission analysis of Earth remote sensing satellites in CDFs. This paper is organized as follows. In the "Remote Sensing Satellites Coverage Analysis" section, the procedure for the determination of the coverage areas is described. The results of the comparison RSS-CA versus STK are included in the "Results" section. Finally, conclusions are summarized in the "Conclusions" section.

Remote Sensing Satellites Coverage Analysis

The RSS-CA methodology for determining the coverage areas of remote sensing satellites is described in this section. RSS-CA can be applied to determine the coverage areas if the geometrical characteristics of the sensor and the attitude of the satellite are known. Additionally, the satellite's orbit needs to be propagated to obtain the Cartesian components of velocity and the subsatellite point of the spacecraft.

Discretization of Observation Areas

The first step of the process is to discretize the areas of interest of the Earth's surface into grid points. To optimize the speed of calculations two assumptions need to be made:

- The Earth's shape is approximated to a sphere, and
- Each area of interest is transformed into its circular projected area on the Earth's surface, called from here on the spherical cap.

Each spherical cap is defined by the latitude and the longitude of its center, ϕ_c and λ_c, and the maximum arc distance $r_{\max}$, as shown in Fig. 3. Accordingly, any point inside the spherical cap will be defined by its latitude and longitude, ϕ and λ.

The geographic coordinate system used to generate the spherical cap grid is the Earth-centered, Earth-fixed (ECEF) Cartesian coordinate system (X_E, Y_E, Z_E) (Zhang et al. 2012; Zhou et al. 1996). First, $\boldsymbol{u_r}$ is defined in the following equation as the vector pointing from the center of the Earth to the center of the coverage area:

$$\boldsymbol{u_r} = \cos\lambda_c \cos\phi_c \boldsymbol{i} + \sin\lambda_c \cos\phi_c \boldsymbol{j} + \sin\phi_c \boldsymbol{k} \tag{1}$$

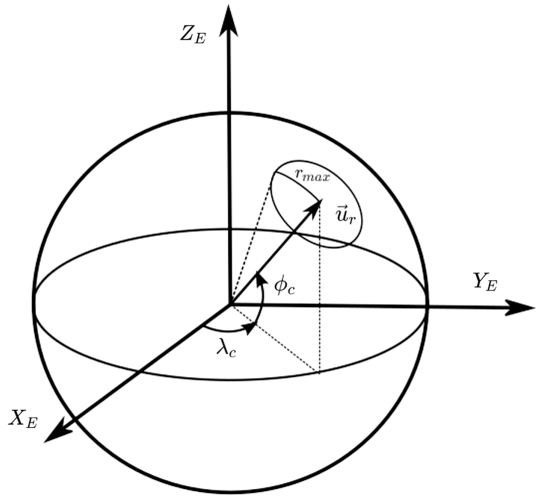

Fig. 3. Area of interest approximated to a spherical cap centered on (λ_c, ϕ_c) with maximum arc distance $r_{\max}$.

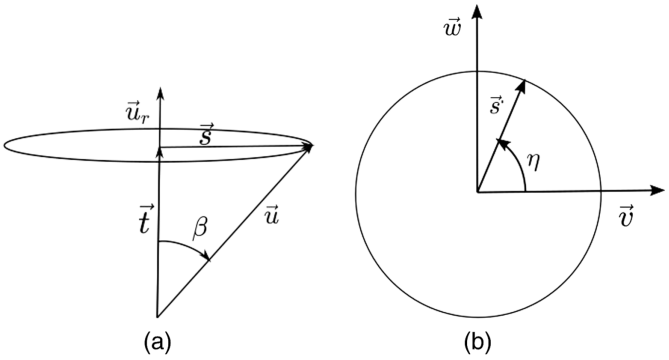

Fig. 4. Construction of a vector pointing from the center of the Earth to the center of the spherical cap: (a) vector $\boldsymbol{u}$ decomposed by parallel and perpendicular vector to $\boldsymbol{u}_r$, $\boldsymbol{t}$ and $\boldsymbol{s}$; and (b) vector $\boldsymbol{s}'$ constructed by ($\boldsymbol{v}$, $\boldsymbol{w}$) basis and angle $\boldsymbol{\eta}$.

Then, the coordinates of the interior points can be obtained by parametrizing a new vector $\boldsymbol{u}$. As shown in Fig. 4(a), vector $\boldsymbol{u}$ can be decomposed in two vectors, $\boldsymbol{t}$, parallel to $\boldsymbol{u_r}$, and $\boldsymbol{s}$, perpendicular to $\boldsymbol{u_r}$

$$\boldsymbol{u} = \boldsymbol{t} + \boldsymbol{s}, \qquad \boldsymbol{t} = \boldsymbol{u_r}\cos\beta, \qquad \boldsymbol{s} = \boldsymbol{s}'\sin\beta \tag{2}$$

where β = angle between the line joining the center of the Earth and the center of the spherical cap (λ_c, ϕ_c) and the line between the center of the Earth and any point inside the spherical cap (at an arc length r from its center)

$$\beta = \frac{r}{R_E} \tag{3}$$

where R_E = radius of the Earth.

Vector $\boldsymbol{s}'$ from Eq. (2) is based on two normalized vectors, $\boldsymbol{v}$ and $\boldsymbol{w}$, and the angle η

$$\boldsymbol{s}' = \boldsymbol{v}\cos\eta + \boldsymbol{w}\sin\eta \tag{4}$$

as shown in both Fig. 4(b) and Eq. (4). Both vectors $\boldsymbol{v}$ and $\boldsymbol{w}$ are tangent to the Earth surface and form a basis with origin in the center of the spherical cap. Vector $\boldsymbol{v}$ is selected as any vector perpendicular to $\boldsymbol{u_r}$, and vector $\boldsymbol{w}$ is calculated perpendicular to $\boldsymbol{v}$ and $\boldsymbol{u_r}$ as

$$\boldsymbol{w} = \frac{\boldsymbol{u_r} \wedge \boldsymbol{v}}{\|\boldsymbol{u_r} \wedge \boldsymbol{v}\|} \tag{5}$$

The following equation summarizes the previous steps to calculate vector $\boldsymbol{u}$ as a function of angles β and η and vectors $\boldsymbol{u_r}$, $\boldsymbol{v}$, and $\boldsymbol{w}$:

$$\boldsymbol{u}(\eta, \beta) = \boldsymbol{u_c} \cos\beta + (\boldsymbol{v} \cos\eta + \boldsymbol{w} \sin\eta) \sin\beta \tag{6}$$

where $\beta \in (0, r_{\max}/R_E]$ and $\eta \in [0, 2\pi)$.

Finally, for each vector $\boldsymbol{u}$, its spherical coordinates can be calculated with the following equations:

$$\phi(\eta, \beta) = \cos^{-1}(u_z) \tag{7}$$

$$\lambda(\eta, \beta) = \cos^{-1}\left(\frac{u_x}{\cos\phi}\right) \tag{8}$$

where λ and ϕ = latitude and the longitude of any point inside the spherical cap; and u_x and $u_z = x$-axis and z-axis components of vector $\boldsymbol{u}$.

Sensor Pointing and Field of View

To analyze the satellite coverage areas, it is necessary to study the sensor pointing and its field of view (FOV). The analysis of the sensor pointing starts constructing two new Cartesian coordinate systems. The first is a local tangent plane coordinate system (X_T, Y_T, Z_T) located at the subsatellite point (of latitude ϕ_{sat} and longitude λ_{sat}), as shown in Fig. 5.

Unit vectors of the local tangent plane coordinate systems are calculated as follows:

$$\boldsymbol{u}_{X_T} = \begin{bmatrix} -\sin\lambda_{\text{sat}} \\ \cos\lambda_{\text{sat}} \\ 0 \end{bmatrix} \tag{9}$$

$$\boldsymbol{u}_{Y_T} = \begin{bmatrix} -\cos\lambda_{\text{sat}} \sin\phi_{\text{sat}} \\ -\sin\lambda_{\text{sat}} \sin\phi_{\text{sat}} \\ \cos\phi_{\text{sat}} \end{bmatrix} \tag{10}$$

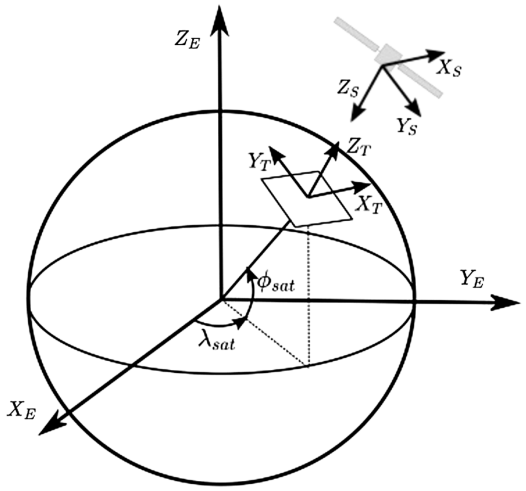

Fig. 5. Local tangent plane and sensor reference frames constructed from the subsatellite point (λ_{sat}, ϕ_{sat}).

$$\boldsymbol{u}_{Z_T} = \begin{bmatrix} \cos\lambda_{\text{sat}} \cos\phi_{\text{sat}} \\ \sin\lambda_{\text{sat}} \cos\phi_{\text{sat}} \\ \sin\phi_{\text{sat}} \end{bmatrix} \tag{11}$$

where the X_T-axis is tangent to the local parallel and points toward the east; the Y_T-axis is tangent to the local meridian and points toward the north; and the Z_T-axis completes the triad and points toward the zenith.

The second Cartesian coordinate system (X_S, Y_S, Z_S) is shown in Fig. 5 and is defined assuming that the sensor is centered on the center of gravity (CoG) of the satellite (i.e., the origin of the coordinate system coincides with the satellite CoG). The unit vectors are defined as

$$\boldsymbol{u}_{X_S} = \boldsymbol{u}_{X_T} \tag{12}$$

$$\boldsymbol{u}_{Y_S} = -\boldsymbol{u}_{Y_T} \tag{13}$$

$$\boldsymbol{u}_{Z_S} = -\boldsymbol{u}_{Z_T} \tag{14}$$

where the X_S-axis has the same direction of X_T; the Z_S-axis has the opposite direction of Z_T; and the Y_S-axis completes the triad.

The pointing direction of the sensor, $\boldsymbol{u}_p$, is defined in Fig. 6(a). It deviates from the nadir direction by an angle γ and, on the (X_S, Y_S) plane projection, is also tilted from the X_S-axis an angle ε. The angle ε

$$\varepsilon = \nu + \delta \tag{15}$$

which is shown in Fig. 6(b), is considered to be composed of two additional angles, ν, and δ, where ν corresponds to the apparent angle between the satellite velocity and the local parallel of the Earth, and δ is the angle between the pointing direction of the sensor and the velocity on the (X_S, Y_S)-plane projection. Angle ν changes with time and depends on the position of the satellite in its orbit; both δ and γ depend on the satellite attitude so they can be modified to fulfill the pointing requirements. Angle ν is defined as

$$\nu = -\tan^{-1}\left(\frac{\|\boldsymbol{V}_{Y_T}\|}{\|\boldsymbol{V}_{X_T}\|}\right) \tag{16}$$

where $\boldsymbol{V}_{X_T}$ and $\boldsymbol{V}_{Y_T}$ = satellite velocities along X_T- and Y_T-directions, respectively. If the satellite velocity in Cartesian components is defined as $\boldsymbol{V} = V_x\boldsymbol{i} + V_y\boldsymbol{j} + V_z\boldsymbol{k}$, its projection along X_T and Y_T axes can be expressed as

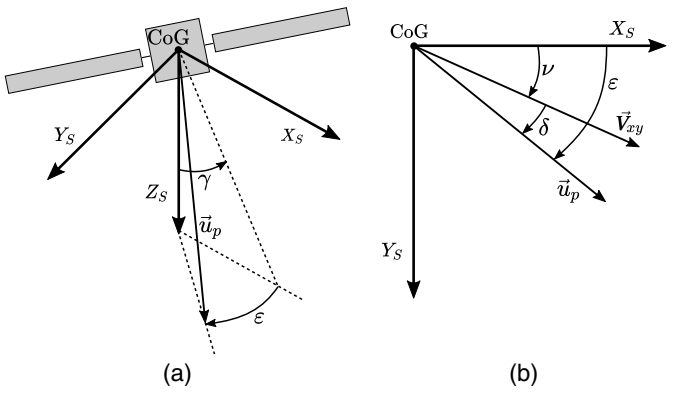

Fig. 6. (a) sensor pointing direction as a function of angles γ and ε; and (b) sensor pointing direction on $X_S Y_S$-plane as a function of angles ν and δ.

$$\boldsymbol{V}_{X_T} = (\boldsymbol{V} \bullet \boldsymbol{u}_{X_T})\boldsymbol{u}_{X_T} \tag{17}$$

$$\boldsymbol{V}_{Y_T} = (\boldsymbol{V} \bullet \boldsymbol{u}_{Y_T})\boldsymbol{u}_{Y_T} \tag{18}$$

where $\boldsymbol{V}$ = satellite velocity; and $\boldsymbol{u}_{X_T}$ and $\boldsymbol{u}_{Y_T}$ = unit vectors along the X_T- and Y_T-axes. Using Eqs. (9) and (10), angle ν can be finally expressed in spherical coordinates as

$$\nu = \tan^{-1}\left(\frac{-\cos\lambda\sin\phi V_x - \sin\lambda\sin\phi V_y + \cos\phi V_z}{-\sin\lambda V_x + \cos\lambda V_y}\right) \tag{19}$$

Conical Sensors

Conical sensors are widely used for Earth observation missions. Some examples of this sensors are the Advanced Very High Resolution Radiometer (AVHRR) of the National Oceanic and Atmospheric Administration (NOAA) (Domenikiotis et al. 2003) and the microwave radiometers on Sentinel 3 (Palacios Lazaro et al. 2014). These sensors are mainly characterized by their antenna half-power beams and, henceforth, semiaperture angle or α_c. Fig. 7 shows the conical sensor FOV.

Considering that the sensor points to the nadir, its FOV can be modeled with the unit vector function $\boldsymbol{u}^S_{C,0}$, described in Eq. (20)

$$\boldsymbol{u}^S_{C,0}(\theta,\alpha) = \sin\alpha\begin{bmatrix}\cos\theta\\ \sin\theta\\ \cot\alpha\end{bmatrix} \tag{20}$$

The vector $\boldsymbol{u}^S_{C,0}$ points toward any observable direction of the sensor and can be parameterized by the angles θ and α. Angle α takes values between 0 and the conical semiaperture angle of the sensor, α_c, and angle θ between 0 and 2π.

The off-nadir pointing of the sensor is taken into account by transforming $\boldsymbol{u}^S_{C,0}$ with the following rotation matrices:

$$\mathbf{R}_y(\gamma) = \begin{pmatrix}\cos\gamma & 0 & \sin\gamma\\ 0 & 1 & 0\\ -\sin\gamma & 0 & \cos\gamma\end{pmatrix} \tag{21}$$

$$\mathbf{R}_z(\varepsilon) = \begin{pmatrix}\cos\varepsilon & -\sin\varepsilon & 0\\ \sin\varepsilon & \cos\varepsilon & 0\\ 0 & 0 & 1\end{pmatrix} \tag{22}$$

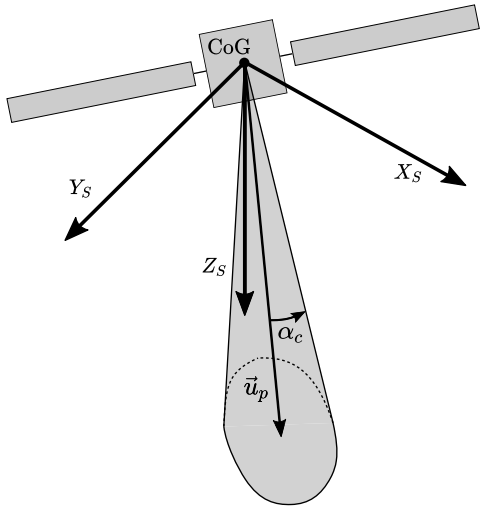

Fig. 7. Geometry of a conical sensor FOV.

where angles γ and ϵ are shown in Fig. 6(a). Using rotation matrices $\mathbf{R}_y$ and $\mathbf{R}_z$, the observable directions of an off-nadir conical sensor is given by

$$\boldsymbol{u}^S_C(\theta,\alpha) = \mathbf{R}_z(\varepsilon)\mathbf{R}_y(\gamma)\boldsymbol{u}^S_{C,0}(\theta,\alpha) \tag{23}$$

In addition, for certain combinations between the orbit altitude, the off-nadir angle, γ, and the semiaperture angle of the conical sensor, α_c, a fraction of the sensor FOV could exceed the local horizon of the Earth, in a situation as depicted in Fig. 8.

In order to determine which observable directions of the sensor exceed the Earth's horizon, an angle μ_C is defined. This is the angle between the Z_S-axis and any direction within the FOV of the sensor, i.e., $\mu_C \in [(\gamma-\alpha_c),(\gamma+\alpha_c)]$ (as inferred from Fig. 8). Any observable direction in wich the angle μ_C is greater than $\mu_{\max}$, does not intersect the Earth. The value of $\mu_{\max}$ depends on the satellite altitude and can be calculated by using the following equation:

$$\mu_{\max} = \sin^{-1}\left(\frac{R_E}{R_E+h}\right) \tag{24}$$

where R_E = Earth radius; and h = orbit altitude. Angle μ_{Cc} can be expressed as a function of γ, α, and θ as

$$\mu_C = \cos^{-1}(\cos\gamma\cos\alpha - \sin\gamma\cos\theta\sin\alpha) \tag{25}$$

As shown in Fig. 8, μ_C can take values as high as $\gamma+\alpha_c$. As long as $\mu_{\max} \geq \gamma+\alpha_c \quad \forall\,\theta$, the FOV of the conical sensor is always observing the Earth (within the local horizon).

On the other hand, a value of $\theta=\theta_i$ could exist so $\mu_{\max} < \mu(\theta_i,\alpha_c)$. For this case, a maximum value of α, $\alpha_{i,\max}$, can be calculated from

$$\mu_{\max} = \cos^{-1}(\cos\gamma\cos\alpha_{i,\max} - \sin\gamma\cos\theta_i\sin\alpha_{i,\max}) \tag{26}$$

where Eq. (26) is a particularization of Eq. (25) for $\mu_{\max}$ and θ_i and allows the calculation of the maximum semiaperture angle of the sensor that ensures an FOV observing the Earth. Therefore, for each θ_i value (between 0 and 2π), angle α could be restricted to $\alpha_{i,\max}$, a limit value, which is lower than the sensor conical semiaperture angle, α_c.

Additionally, for each θ_i, the actual semiaperture angle takes values between 0 and the minimum between $\alpha_{i,\max}$ and α_c. An example of a conical FOV domain is shown in Fig. 9. For the given

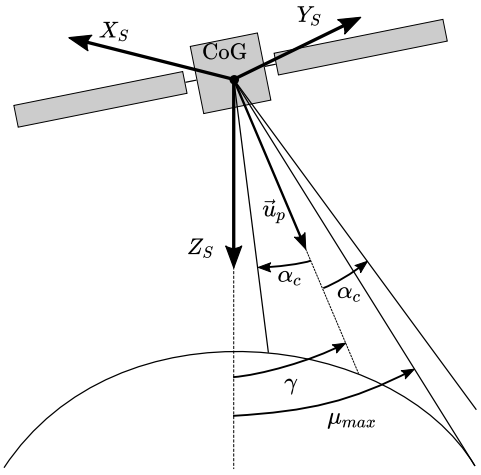

Fig. 8. Off-nadir pointing of a conical sensor exceeding Earth's horizon.

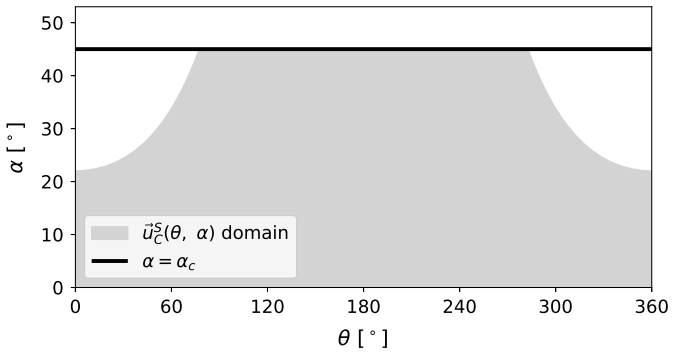

Fig. 9. Domain of a conical FOV with $\alpha_c = 45°$ and $\gamma = 45°$ in a 500-km orbit altitude.

example and according to Eq. (24), the maximum off-nadir angle for observing the Earth is approximately 68°. Because the maximum off-nadir angle of the sensor FOV is 90°, it is clear that some observable directions do not intersect the Earth. As a result, the α values are restricted for θ values between −75° and 75°.

Finally, $\boldsymbol{u}_C^S$ must be expressed in ECEF axes for further calculations. This can be done by transforming $\boldsymbol{u}_C^S$ as

$$\boldsymbol{u}_C = \mathbf{P}_{S\to E}\boldsymbol{u}_C^S \tag{27}$$

where $\mathbf{P}_{S\to E}$ is the rotation matrix from the (X_S, Y_S, Z_S) coordinate system to the (X_E, Y_E, Z_E) coordinate system and is given by

$$\mathbf{P}_{S\to E} = [\boldsymbol{u}_{X_S}, \quad \boldsymbol{u}_{Y_S} \quad , \boldsymbol{u}_{Z_S}] \tag{28}$$

Rectangular Sensors

Rectangular sensors are widely used for remote sensing applications, examples being the Multispectral Instrument (MSI) on Sentinel-2 (Drusch et al. 2012) and the Thermal Infrared Sensor (TIRS) on Landsat-8 (Barsi et al. 2014). These sensors are geometrically defined by their along-track and cross-track semiaperture angles, α_h and α_v, respectively. Fig. 10 shows the geometry of a rectangular sensor FOV. Once more, considering that the sensor points to the nadir, its FOV is modeled with the unit vector function $\boldsymbol{u}_{R,0}^S$ given by

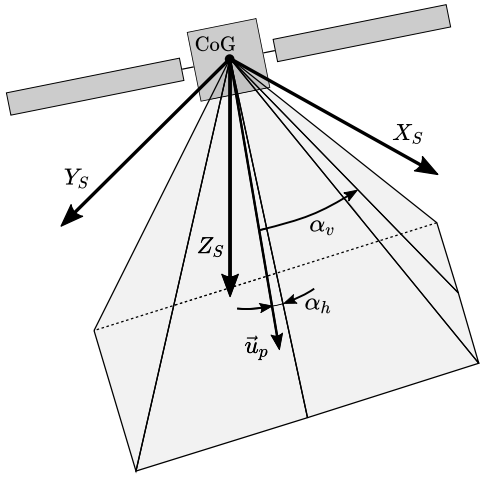

Fig. 10. Geometry of a rectangular sensor FOV.

$$\boldsymbol{u}_{R,0}^S(\alpha_x,\alpha_y) = \frac{1}{\sqrt{1+\tan^2\alpha_x+\tan^2\alpha_y}}\begin{bmatrix}\tan\alpha_x\\ \tan\alpha_y\\ 1\end{bmatrix} \tag{29}$$

The vector $\boldsymbol{u}_{R,0}^S$ points toward any observable direction of the sensor and can be parameterized by the angles α_x and α_y. Angle α_x takes values between $\pm\alpha_h$, and angle α_y between $\pm\alpha_v$. Again, $\boldsymbol{u}_{R,0}^S$ must be transformed with the rotation matrices defined in Eqs. (21) and (22). Thus, the observable directions of an off-nadir rectangular sensor are calculated with

$$\boldsymbol{u}_R^S(\alpha_x,\alpha_y) = \mathbf{R}_z(\varepsilon)\mathbf{R}_y(\gamma)\boldsymbol{u}_{R,0}^S(\alpha_x,\alpha_y) \tag{30}$$

As in the case of the conical sensor, for certain combinations between the orbit altitude, the off-nadir angle γ, and the semiaperture angles α_h and α_v, a portion of the rectangular sensor FOV could exceed the Earth's horizon. The angle between the Z_S-axis and any direction within the FOV of the rectangular sensor is given by

$$\mu_R = \cos^{-1}\left(\frac{-\sin\gamma\tan\alpha_x+\cos\gamma}{\sqrt{1+\tan^2\alpha_x+\tan^2\alpha_y}}\right) \tag{31}$$

According to Eq. (31), μ_R takes values between $\mu_{R_{\min}}$ and $\mu_{R_{\max}}$, with these values calculated as in the following equations:

$$\mu_{R_{\min}} = \begin{cases}\mu_R(\alpha_x=-\alpha_h,\alpha_y=0) & \text{if } |\gamma-\alpha_h|\geq\alpha_v\\ \mu_R(\alpha_x=0,\alpha_y=\alpha_v) & \text{if } |\gamma-\alpha_h|<\alpha_v\end{cases} \tag{32}$$

$$\mu_{R_{\max}} = \mu_R(\alpha_x=\alpha_h,\alpha_y=\alpha_v) \tag{33}$$

As long as $\mu_{R_{\max}} \leq \mu_{\max}$, the complete FOV of the rectangular sensor observes the Earth. However, if the previous condition is not met, the domain of $\boldsymbol{u}_R^S$ must be determined. This procedure starts calculating the maximum and minimum values of α_x. From Eq. (31) it can be concluded that $\tan^2\alpha_y$ is given by

$$\tan^2\alpha_y = \left(\frac{\cos\gamma-\sin\gamma\tan\alpha_x}{\cos\mu_{\max}}\right)^2-(1+\tan^2\alpha_x) \tag{34}$$

The expression of the right side of Eq. (34) has to be equal to or greater than zero, so the valid values of α_x can be obtained by solving for α_x with the following quadratic inequality:

$$\left(\frac{\cos\gamma-\sin\gamma\tan\alpha_x}{\cos\mu_{\max}}\right)^2-(1+\tan^2\alpha_x)\geq 0 \tag{35}$$

Then, α_x takes values between $\alpha_{x_{\min}}$ and $\alpha_{x_{\max}}$, with these angles computed with

$$\alpha_{x_{\min}} = \max\{-\alpha_h,-(\gamma+\mu_{\max})\} \tag{36}$$

$$\alpha_{x_{\max}} = \min\{\alpha_h,(\mu_{\max}-\gamma)\} \tag{37}$$

Additionally, for each α_{x_i} between $\alpha_{x_{\min}}$ and $\alpha_{x_{\max}}$, it is possible to derive the value of α_{y_i}

$$\alpha_{y_i} = \pm\tan^{-1}\left(\sqrt{\left(\frac{\cos\gamma-\sin\gamma\tan\alpha_{x_i}}{\cos\mu_{\max}}\right)^2-(1+\tan^2\alpha_{x_i})}\right) \tag{38}$$

Then, the maximum and minimum values of α_{y_i} can be calculated with the following equations:

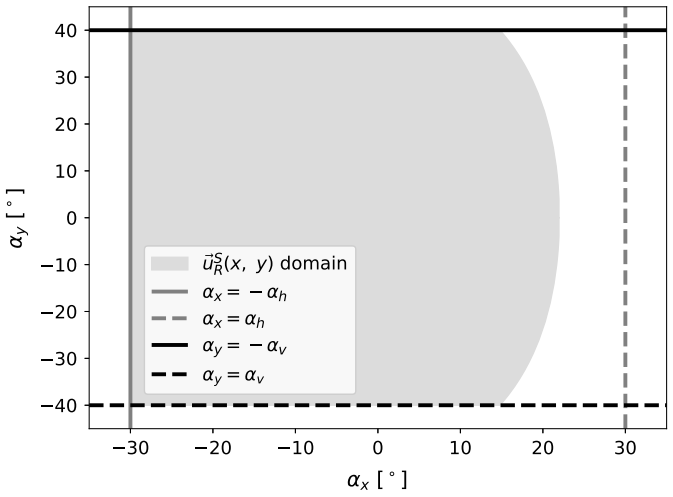

Fig. 11. Domain of a rectangular FOV with $\alpha_h = 30°$, $\alpha_v = 40°$, and $\gamma = 45°$, in a 500-km orbit altitude.

$$\alpha_{y_{\min},i} = \max\{-\alpha_v, \min(\alpha_{y_i})\} \tag{39}$$

$$\alpha_{y_{\max},i} = \min\{\alpha_h, \max(\alpha_{y_i})\} \tag{40}$$

An example of a rectangular FOV domain is shown in Fig. 11. For the given example and according to Eq. (24), the maximum off-nadir angle for observing the Earth is approximately 68°. Because the maximum off-nadir angle of the sensor FOV is 77.9°, it is clear that some observable directions do not intersect the Earth. As a result, positive values of α_x must be less than α_h. Finally, in order to express $\boldsymbol{u}_R^S$ in ECEF axes, $\boldsymbol{u}_R^S$ is transformed as follows:

$$\boldsymbol{u}_R = \mathbf{P}_{S\to E}\boldsymbol{u}_R^S \tag{41}$$

where $\mathbf{P}_{S\to E}$ is determined by Eq. (28).

Satellite Viewing Area and Coverage

The areas of the Earth's surface observed by the sensor are calculated solving the sphere-line intersection problem, i.e., by calculating the intersection between the Earth's surface and the sensor FOV. The sphere-line intersection problem is expressed by the following system of equations:

$$\begin{aligned} &\|\boldsymbol{r}_i\| = R_E \\ &\boldsymbol{r}_i = \boldsymbol{r}_{\text{sat}} + \kappa\boldsymbol{u}_{s,i} \end{aligned} \tag{42}$$

where $\boldsymbol{u}_{s,i}$ is the unitary vector of any observable direction expressed in ECEF axes; $\boldsymbol{r}_{\text{sat}}$ = satellite position; and R_E = Earth's radius. The following equation can be derived from Eq. (42) and solved for κ, choosing the lowest root solution:

$$\kappa^2 - (2\boldsymbol{r}_{\text{sat}} \bullet \boldsymbol{u}_{s,i})\kappa + \|\boldsymbol{r}_{\text{sat}}\|^2 - R_E^2 = 0 \tag{43}$$

Finally, the spherical coordinates of the corresponding FOV line can be calculated with

$$\lambda_i = \tan^{-1}\left(\frac{r_{y_i}}{r_{x_i}}\right) \tag{44}$$

$$\phi_i = \sin^{-1}\left(\frac{r_{z_i}}{R_E}\right) \tag{45}$$

where $(r_{x_i}, r_{y_i}, r_{z_i})$ are the Cartesian components of vector $\boldsymbol{r}_i$.

In order to quantify the deviations of the viewing area of the proposed method with respect to others, the following error analysis was carried out. Let $\boldsymbol{r}_i$ and $\boldsymbol{r}_j^*$ be any point of the viewing area border calculated with the present method and any reference point obtained with another method, respectively. The Earth's central angle between $\boldsymbol{r}_i$ and $\boldsymbol{r}_j^*$ is calculated as follows:

$$\rho = \cos^{-1}\left(\frac{\boldsymbol{r}_i \bullet \boldsymbol{r}_j^*}{\|\boldsymbol{r}_i\|\|\boldsymbol{r}_j^*\|}\right) \tag{46}$$

Then, the distance between these two points (great-circle distance), E_{ij}, is given by

$$E_{ij} = \rho R_E \tag{47}$$

The deviation of each calculated border point, E_i, is assumed to be equal to the lowest distance to the reference border

$$E_i = \min(E_{ij}) \tag{48}$$

These deviations are a consequence of the perfect spherical Earth assumption and increase for the following reasons: (1) high aperture angle and/or high off-nadir angle of the sensor, (2) high orbit altitude, and (3) observation of places near the equator or the geographical poles, where the local Earth's radius differs with the Earth's mean radius (6,371 km). Because all of these effects play an important role in the observed area, A, it can be included in the error analysis to compare the deviations for different orbit, sensor geometry, and pointing cases. In this particular error analysis, the minimum distance defined previously, E_i, is dimensionalized with the following equation:

$$e_i = \frac{E_i}{l} \tag{49}$$

where e_i = dimensionless error based on a characteristic length, l, defined by the square root of the observed area

$$l = \sqrt{A} \tag{50}$$

Finally, the mean value and the standard deviation of the dimensionless error, $\bar{e}$ and σ, respectively are given by

$$\bar{e} = \frac{\sum_{i=1}^{n} e_i}{n} \tag{51}$$

$$\sigma = \sqrt{\frac{\sum_{i=1}^{n} (e_i - \bar{e})^2}{n-1}} \tag{52}$$

where n = number of calculated border points of the observed area.

The case of a satellite with an elliptic orbit was defined to check the accuracy of the proposed methodology RSS-CA. This orbit is defined by 400- and 1,000-km perigee and apogee altitudes and a 60° inclination. The viewing geometry was computed with RSS-CA and compared with the results obtained with AGI STK. Fig. 12 shows the evolution of the borders of the observed areas by conical and rectangular sensors. Small differences can be observed between the results from both methodologies.

Going one step further, the dimensionless mean distance, $\bar{e}$, and its standard deviation, σ, between the observed areas [Eqs. (51) and (52)], calculated with RSS-CA and STK, are included in Tables 1 and 2 for different altitudes of the satellite within the orbit, equipped with conical and rectangular sensors with two different off-nadir pointing angles, $\gamma = 25°$ and $\gamma = 45°$. Additionally, the values of the dimensionless mean distance, $\bar{e}$, have been also plotted regarding the altitude in the graphs from Fig. 13. In the case of

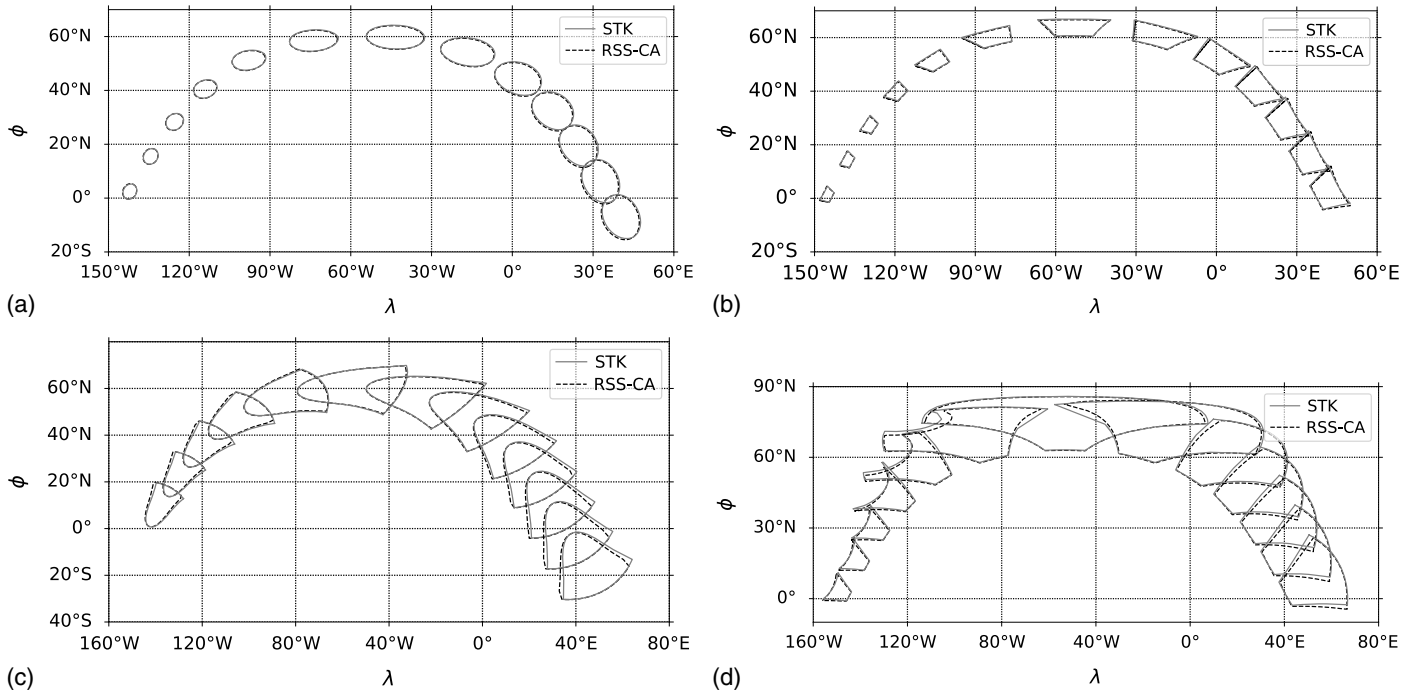

Fig. 12. Evolution of a conical and a rectangular FOV–Earth intersection generated by STK (solid line) and computed with the present method (dashed line) over half an orbit for 25° and 45° off-nadir pointing angles (γ). The inclination, the angle of perigee, and the perigee and apogee altitudes are 60°, 0°, 400 km, and 1,000 km, respectively. The conical sensor has an along-track pointing ($\delta = 0°$) and its semiaperture angle, α_c, is 30°. The rectangular sensor has a cross-track pointing ($\delta = -90°$) and its semiaperture angles, α_h and α_v, are 20° and 30°, respectively: (a) conical sensor with $\gamma = 25°$; (b) rectangular sensor with $\gamma = 25°$; (c) conical sensor with $\gamma = 45°$; and (d) rectangular sensor with $\gamma = 45°$.

Table 1. Dimensionless mean percentage error, $\bar{e}$, and standard deviation, σ, of conical and rectangular sensor viewing areas as a function of the orbit altitude for 25° off-nadir pointing angle (γ)

h (km)	$\bar{e}_{CS}$ (%)	σ_{CS} (%)	$\bar{e}_{RS}$ (%)	σ_{RS} (%)
406.65	2.33	1.12	3.23	1.62
416.08	1.96	0.79	3.86	1.99
443.94	2.03	0.64	4.33	2.13
488.91	2.11	0.83	4.32	1.75
547.91	2.00	0.81	3.97	1.13
617.67	1.78	0.78	3.18	1.05
694.61	1.83	0.78	2.59	1.31
772.36	2.10	0.83	2.86	1.02
847.47	2.54	1.00	3.29	1.29
912.66	2.79	1.14	3.56	1.70
963.68	2.91	1.31	3.78	1.94
996.09	2.92	1.36	3.81	2.00
1,007.65	2.73	1.25	3.61	1.93

Note: CS and RS subscripts denote conical and rectangular sensor, respectively. The orbit inclination is 60°, the angle of perigee is 0°, and the initial and final altitudes correspond with the perigee and apogee. The conical sensor has an along-track pointing ($\delta = 0°$) and its semiaperture angle, α_c, is 30°. The rectangular sensor has a cross-track pointing ($\delta = -90°$) and its semiaperture angles, α_h and α_v, are 20° and 30°, respectively.

Table 2. Dimensionless mean percentage error, $\bar{e}$, and standard deviation, σ, of conical and rectangular sensor viewing areas as a function of the orbit altitude for 45° off-nadir pointing angle (γ)

h (km)	$\bar{e}_{CS}$ (%)	σ_{CS} (%)	$\bar{e}_{RS}$ (%)	σ_{RS} (%)
406.65	2.47	2.04	3.74	2.68
416.08	2.12	1.63	3.91	2.71
443.94	2.02	1.55	3.93	2.71
488.91	1.85	1.38	3.84	3.05
547.91	1.70	1.25	3.15	2.57
617.67	1.63	1.43	2.87	3.02
694.61	1.70	1.65	1.96	1.78
772.36	1.85	1.71	2.23	2.24
847.47	1.99	1.37	2.34	1.67
912.66	2.29	1.75	2.66	2.05
963.68	2.32	0.14	2.89	2.39
996.09	2.44	1.65	2.95	2.30
1,007.65	2.52	2.31	2.88	2.28

Note: CS and RS subscripts denote conical and rectangular sensor, respectively. The orbit inclination is 60°, the angle of perigee is 0°, and the initial and final altitudes correspond with the perigee and apogee. The conical sensor has an along-track pointing ($\delta = 0°$) and its semiaperture angle, α_c, is 30°. The rectangular sensor has a cross-track pointing ($\delta = -90°$) and its semiaperture angles, α_h and α_v, are 20° and 30°, respectively.

the conical sensor with a $\gamma = 25°$ off-nadir pointing angle, the average dimensionless distances between RSS-CA and STK observed areas are 1.8% to 2.9% of the characteristic length (which can be reasonably considered as the width of the observed area). These dimensionless distances are 2.6% to 4.3% if a rectangular sensor is considered, whereas if a $\gamma = 45°$ off-nadir pointing angle is considered instead of $\gamma = 25°$, the dimensionless mean distances between RSS-CA and STK observed areas are 1.6% to 2.5% (conical sensors) and 2.0% to 3.9% (rectangular sensors).

Additionally, if the calculated values of the standard deviation, σ, are taken into account, the 1–sigma (68% confidence level) bracket around the average distance, $\bar{e}$, can be defined (assuming a Gaussian distribution). The upper limit of these brackets is also plotted for each case in the graphs in Fig. 13. These new points

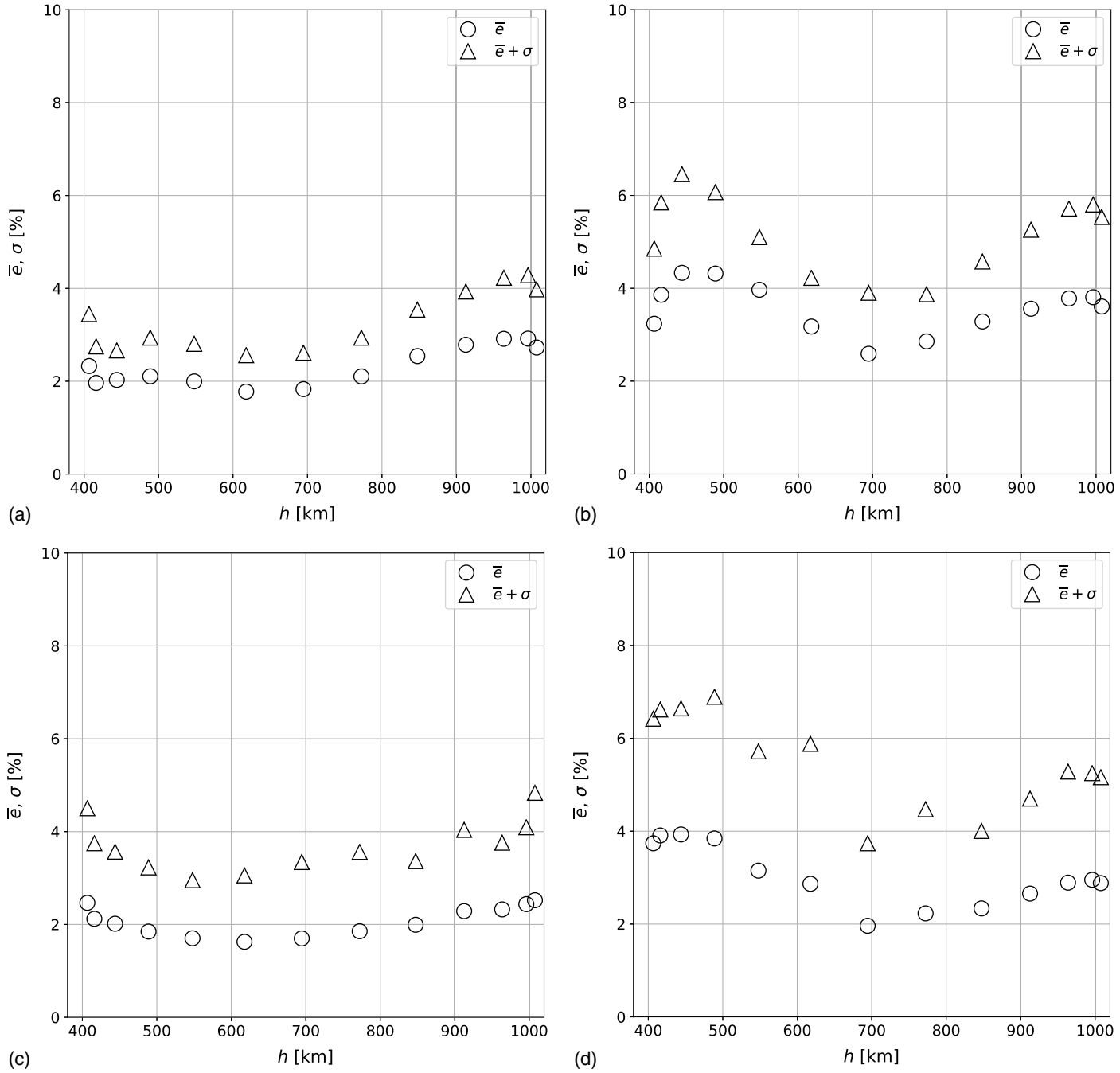

Fig. 13. Dimensionless mean percentage error, $\bar{e}$, and standard deviation, σ, of conical and rectangular sensor viewing areas as a function of the orbit altitude for 25° and 45° off-nadir pointing angles (γ). The orbit inclination is 60°, the angle of perigee is 0°, and the initial and the final altitudes correspond with the perigee and apogee. The conical sensor has an along-track pointing ($\delta = 0°$) and its semiaperture angle, α_c, is 30°. The rectangular sensor has a cross-track pointing ($\delta = -90°$) and its semiaperture angles, α_h and α_v, are 20° and 30°, respectively: (a) conical sensor with $\gamma = 25°$; (b) rectangular sensor with $\gamma = 25°$; (c) conical sensor with $\gamma = 45°$; and (d) rectangular sensor with $\gamma = 45°$.

represent the maximum distance between the border points from RSS-CA and STK observed areas with a 68% confidence level.

The effect of the off-nadir pointing inclination is not noticeable according to the data from Table 1 and Fig. 13. Additionally, for low altitudes (very close to 400 km in the case of the conical sensor) the 68% confidence limit of the distance between the borders of the observed areas from RSS-CA and STK (i.e., the value of $\bar{e}$ plus σ) seems to be higher in relation to the ones from higher altitudes at $h = 600$ km. From this point to $h = 1{,}000$ km, the 68% confidence limit distance between the observed areas tends to increase up to 5%–6% of the characteristic length, depending on the case.

According to these results, it seems reasonable to assume a good match of the observed area calculated by the RSS-CA methodology described in this paper and the one from STK, with a reduced impact of the spherical Earth assumption.

The accesses of a satellite sensor to an area of interest are achieved when the sensor FOV intersects the aforementioned area. Considering a spherical cap, the targeted area is observed by the sensor when the following condition is met:

$$\boldsymbol{u}_r \bullet \frac{\boldsymbol{r}_i}{\|\boldsymbol{r}_i\|} \geq \cos\beta(r_{\max}) \tag{53}$$

where angle $\beta(r_{\max})$ is determined by Eq. (3); and $r_{\max}$ is the maximum arc distance from the center of the studied area.

Finally, the coverage of the satellite at any time can be obtained as the percentage of the targeted area seen by the sensor. An analytical expression to compute the coverage is beyond the scope of this study due to the complexity of the intersection areas. The proposed method consists of computing a large amount of viewed points, $\boldsymbol{r}_i$, and then selecting the ones that meet Eq. (53). Then the covered area of the target, A_t, is calculated numerically and the coverage is obtained as follows:

$$\text{coverage} = \frac{A_t}{2\pi R_E^2(1-\cos\beta)} \times 100\% \tag{54}$$

Results

The method presented in this paper for analyzing the coverage area of remote sensing sensors on board LEO satellites is validated by comparison to simulations performed with AGI STK. The case study selected to assess the accuracy of the method is the MARTINLARA mission.

Because the observation of the magnetic poles is of great interest, a spherical cap around them has been defined to study satellite coverage. These areas can be seen in Fig. 14 as gray shaded areas, where the coordinates of the north and south magnetic poles are marked with symbols + and –, respectively. The parameters used to define the spherical cap (as defined in the "Remote Sensing Satellites Coverage Analysis" section) are included in Table 3.

Three study cases are presented in this section for validating the method (Table 4). In all cases, dawn-dusk sun-synchronous orbits were used in order to fulfill illumination requirements.

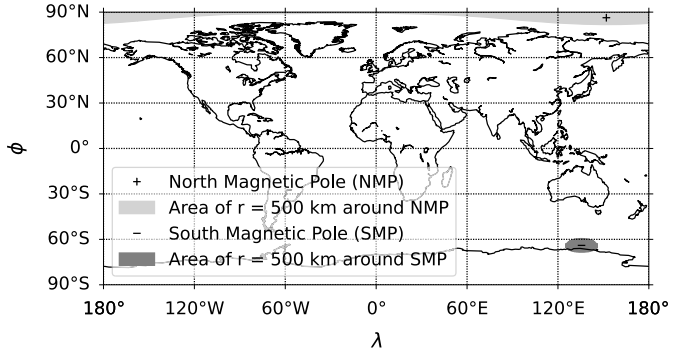

Fig. 14. Equidistant cylindrical projected world map indicating the estimated geographic location of the magnetic poles in 2022 and the areas of 500 km (spherical caps) around them. Magnetic poles data from National Oceanic and Atmospheric Administration (2016).

Table 3. Parameters to define the area of interest of the study cases

Magnetic pole	λ_c (degrees)	ϕ_c (degrees)	r (km)
North	151.95	86.29	500
South	135.57	−63.98	500

Table 4. Parameters of Study Cases 1, 2, and 3

Case	h (km)	δ (degrees)	γ (degrees)	α_c (degrees)
1	450	90	5	3.2
2	500	90	10	2.8
3	550	90	15	2.4

Also, because the sensors are radiometers, they were modeled as conical sensors. The study cases differ in the orbit altitude, h, the off-nadir pointing, γ, and the semiaperture angle of the antennas of the radiometers, α_c. The selection of the altitudes was based on the launch opportunities.

According to the mission requirement document (MRD) of the MARTINLARA mission (IDR/UPM Institute 2020), the solar radiation cannot intersect the FOV of the antennas of the radiometers. For zenith-pointing antennas, the illumination condition will limit the number of operational days of the radiometers. Although different geometries for the zenith face are being studied to maximize the number of operation days, they are not presented in this work.

For nadir-pointing antennas (located in the Earth-pointing face of the satellite), this restriction is ensured by tilting the whole satellite by an angle γ. Although the scientific requirements of the mission restrict γ to a maximum value of 5°, the study cases presented here include off-nadir angles of 10° and 15° to assess if increased γ angles could improve the performances of the radiometers. For the semiaperture angle of the antennas, α_c, they are designed to produce a footprint with a maximum semimajor axis of 25 km, in accordance with the MRD.

As in a dawn-dusk sun-synchronous orbit, the velocity of the satellite is quasi-perpendicular to the solar radiation and the satellite must be rotated around the velocity vector. Because the pointing direction is perpendicular to the velocity, the angle δ must be equal to 90°. In addition, because the north magnetic pole is located at a latitude higher than the maximum latitude of the satellite passes, an off-nadir pointing with $\delta = 90°$ ensures the observation of the north magnetic pole.

After the definition of the targeted areas, the altitude of the dawn-dusk orbits, and the sensor properties and pointing, the three orbits were propagated for a whole year with the presence of the J2 perturbation using STK. Then, the accesses were computed with STK and with the RSS-CA method.

The main coverage statistics of the north and south magnetic poles for all the study cases are given in Tables 5 and 6, respectively. As shown in these tables, the comparison between STK and

Table 5. NA, TAT, and MAT for the north magnetic pole, obtained with STK and the RSS-CA method

Case	Source	NA	TAT (h)	MAT (s)
1	STK	1,740	42.20	87.32
	RSS-CA	1,723 (−0.98%)	41.64 (−1.33%)	87.00 (−0.37%)
2	STK	1,870	48.96	94.25
	RSS-CA	1,851 (−1.02%)	48.17 (−1.61%)	93.69 (−0.59%)
3	STK	2,046	57.80	101.71
	RSS-CA	2,025 (−1.03%)	56.80 (−1.73%)	100.97 (−0.73%)

Note: The percentage variation from STK is given in parentheses.

Table 6. NA, TAT, and MAT for the south magnetic pole, obtained with STK and the RSS-CA method

Case	Source	NA	TAT (h)	MAT (s)
1	STK	719	22.72	113.77
	RSS-CA	721 (−0.28%)	22.71 (−0.04%)	113.38 (−0.34%)
2	STK	714	22.81	115.01
	RSS-CA	711 (−0.42%)	22.79 (−0.09%)	115.37 (0.31%)
3	STK	717	23.08	115.91
	RSS-CA	714 (−0.42%)	23.05 (−0.13%)	116.24 (0.29%)

Note: The percentage variation from STK is given in parentheses.

RSS-CA results presents differences in the determination of the number of accesses (NA), total access time (TAT), and mean access time (MAT) between 0.37% and 1.73% for the north magnetic pole and between 0.04% and 0.42% for the south magnetic pole observation.

The discrepancies between STK and RSS-CA simulations are founded on the assumption of a spherical Earth by the RSS-CA method because that affects the construction of the spherical cap and the sensor-viewed areas. Additionally, the orbit was calculated with a self-made orbit propagator so the orbital positions and velocities presented small differences with respect to the ones obtained with STK.

Therefore, the computation of the accesses by RSS-CA is very accurate and it can be a method to be used within the CDF for preliminary design of remote sensing space missions.

Conclusions

This paper presents a method developed for obtaining the coverage area of Earth remote sensing satellites. For a selected area of interest, a simple spherical discretization was carried out by the definition of only three parameters: the longitude and latitude of its center and the arc distance to the perimeter. The pointing geometry of the satellite and the conical and rectangular sensors' FOV are explained in detail. The pointing direction of the satellite is defined with two design or operational parameters: the off-nadir angle and the pointing deviation from the velocity vector. Conical and rectangular sensors are modeled with conical and along-track and cross-track semiaperture angles, respectively. Additionally, for high off-nadir pointing, a procedure for discretizing these angles assuring that the local Earth's horizon is not exceeded is presented.

The sensor viewing area was computed by solving the sphere-line intersection problem. The accesses were obtained by checking if the viewing area intersects the targeted areas and the coverage was computed numerically. The precision of the method was validated by comparison to simulations performed by STK. Three study cases derived from the MARTINLARA mission were used to perform the coverage analysis of the north and south magnetic poles. The compared variables were the number of accesses, the total access time, and the mean access time over a year of operation. The overall results were very successful, with error less than 2.5%.

Finally, the mathematical model presented in this paper is suitable for preliminary mission designs within CDF. The accuracy of this method is comparable to STK. However, it is easy to implement and can be upgraded to include new sensor geometries or even implement algorithms to control the sensor pointing in complex observation missions.

Data Availability Statement

Some or all data, models, or code that support the findings of this study are available from the corresponding author upon reasonable request.

Acknowledgments

This work was partially funded by Comunidad de Madrid S2018/NMT-4333 MARTINLARA-CM. The authors are indebted to the IDR/UPM staff and the members of the MARTINLARA consortium for the support during the development of this work. The authors are also grateful to Project Y2020/NMT-6427 OAPES from the program Sinérgicos 202 from Comunidad de Madrid. Finally, the authors are grateful to the reviewers, whose comments helped to improve this paper.

Notation

The following symbols are used in this paper:

A = total covered area;
A_t = covered area of the target;
E_i = error of a boundary point of the viewed area;
E_{ij} = great-circle distance between a calculated and a reference boundary points;
$\bar{e}$ = dimensionless mean error of the viewed area;
e_i = dimensionless error of a boundary point of the viewed area;
l = characteristic length of the viewed area;
$\mathbf{P}_{S\to E}$ = transformation matrix between sensor coordinate system and geographic coordinate system;
R_E = Earth's mean radius;
$\mathbf{R}_y(\gamma)$ = rotation matrix around the Y_S-axis;
$\mathbf{R}_z(\varepsilon)$ = rotation matrix around the Z_S-axis;
$\boldsymbol{r}_i$ = intersection point of the ith ray of the sensor;
$r_{\max}$ = maximum arc distance from the center of the studied area;
$\boldsymbol{r}_{\text{sat}}$ = satellite position;
$\boldsymbol{u}_C^S$ = conical sensor FOV pointing off-nadir;
$\boldsymbol{u}_{C,0}^S$ = conical sensor FOV pointing to the nadir;
$\boldsymbol{u}_p$ = sensor pointing direction;
$\boldsymbol{u}_R^S$ = rectangular sensor FOV pointing off-nadir;
$\boldsymbol{u}_{R,0}^S$ = rectangular sensor FOV pointing to the nadir;
$\boldsymbol{V}$ = satellite velocity;
$\boldsymbol{V}_{X_T}$ = satellite velocity along X_T-direction;
$\boldsymbol{V}_{Y_T}$ = satellite velocity along Y_T-direction;
X_E, Y_E, Z_E = geographical coordinate system;
X_S, Y_S, Z_S = sensor coordinate system;
X_T, Y_T, Z_T = local tangent plane coordinate system;
α = semiaperture angle of a conical sensor with Z_S-axis;
α_x = semiaperture angle of a rectangular sensor with X_S-axis;
α_y = semiaperture angle of a rectangular sensor with X_Y-axis;
β = angle between the line joining the center of the Earth and the center of the spherical cap and the line between the center of the Earth and any point inside the spherical cap;
γ = off-nadir pointing angle;
δ = angle between $\boldsymbol{u}_p$ and $\boldsymbol{V}$ in the X_SY_S-plane;
ε = angle between $\boldsymbol{u}_p$ and X_S in the X_SY_S-plane;
θ = rotation angle around nadir direction;
λ_c = longitude of the center of the studied area;
λ_i = longitude of the intersection point of the ith ray of the sensor;
λ_{sat} = longitude of the subsatellite point;
μ_C = off-nadir angle of an observable direction of a conical sensor;
$\mu_{\max}$ = maximum off-nadir angle;
μ_R = off-nadir angle of an observable direction of a rectangular sensor;
ν = angle between $\boldsymbol{V}$ and X_S in the X_SY_S-plane;
ρ = Earth's central angle between a calculated and a reference boundary points;

σ = standard deviation of the dimensionless error of the viewed area;
ϕ_c = latitude of the center of the studied area;
ϕ_i = latitude of the intersection point of the i-th of the sensor; and
ϕ_{sat} = latitude of the subsatellite point.

References

Ali, I., N. Al-Dhahir, and J. Hershey. 1999. "Predicting the visibility of LEO satellites." *IEEE Trans. Aerosp. Electron. Syst.* 35 (4): 1183–1190. https://doi.org/10.1109/7.805436.

Bandecchi, M., B. Melton, B. Gardini, and F. Ongaro. 2000. "The ESA/ESTEC concurrent design facility." In *Proc., 2nd European Systems Engineering Conf. (EuSEC 2000)*. San Diego: International Council on Systems Engineering.

Barsi, J. A., J. R. Schott, S. J. Hook, N. G. Raqueno, B. L. Markham, and R. G. Radocinski. 2014. "Landsat-8 thermal infrared sensor (TIRS) vicarious radiometric calibration." *Remote Sens.* 6 (11): 11607–11626. https://doi.org/10.3390/rs61111607.

Bermejo, J., J. Álvarez, P. Arcenillas, E. Roibás-Millán, J. Cubas, and S. Pindado. 2018. "CDF as a tool for space engineering master's student collaboration and concurrent design learning." In *Proc., 8th Int. Systems & Concurrent Engineering for Space Applications Conf. SECESA 2018*. Noordwijk, Netherlands: European Space Agency.

Campbell, J. B., and R. H. Wynne. 2011. *Introduction to remote sensing*. 5th ed. New York: Guilford Press.

Crisp, N., S. Livadiotti, and P. C. E. Roberts. 2018. "A semi-analytical method for calculating revisit time for satellite constellations with discontinuous coverage." Preprint, submitted July 5, 2018. http://arxiv.org/abs/1807.02021.

Cubas, J., A. Farrahi, and S. Pindado. 2015a. "Magnetic attitude control for satellites in polar or sun-synchronous orbits." *J. Guid. Control Dyn.* 38 (10): 1947–1958. https://doi.org/10.2514/1.G000751.

Cubas, J., S. Pindado, and C. De Manuel. 2014a. "Explicit expressions for solar panel equivalent circuit parameters based on analytical formulation and the Lambert w-function." *Energies* 7 (7): 4098–4115. https://doi.org/10.3390/en7074098.

Cubas, J., S. Pindado, and A. Farrahi. 2013. "New method for analytical photovoltaic parameter extraction." In *Proc., 2013 Int. Conf. on Renewable Energy Research and Applications (ICRERA)*, 873–877. Yenimahalle, Ankara: International Journal of Renewable Energy Research.

Cubas, J., S. Pindado, and A. Sanz-Andrés. 2015b. "Accurate simulation of MPPT methods performance when applied to commercial photovoltaic panels." *Sci. World J.* 2015: 1–16. https://doi.org/10.1155/2015/914212.

Cubas, J., S. Pindado, and F. Sorribes-Palmer. 2017. "Analytical calculation of photovoltaic systems maximum power point (MPP) based on the operation point." *Appl. Sci.* 7 (9): 870. https://doi.org/10.3390/app7090870.

Cubas, J., S. Pindado, and M. Victoria. 2014b. "On the analytical approach for modeling photovoltaic systems behavior." *J. Power Sources* 247 (Feb): 467–474. https://doi.org/10.1016/j.jpowsour.2013.09.008.

Cui, H., and C. Han. 2011. "Satellite constellation configuration design with rapid performance calculation and ordinal optimization." *Chin. J. Aeronaut.* 24 (5): 631–639. https://doi.org/10.1016/S1000-9361(11)60074-5.

Domenikiotis, C., A. Loukas, and N. R. Dalezios. 2003. "The use of NOAA/AVHRR satellite data for monitoring and assessment of forest fires and floods." *Nat. Hazards Earth Syst. Sci.* 3 (1–2): 115–128. https://doi.org/10.5194/nhess-3-115-2003.

Drusch, M., et al. 2012. "Sentinel-2: ESA's optical high-resolution mission for GMES operational services." *Remote Sens. Environ.* 120 (May): 25–36. https://doi.org/10.1016/j.rse.2011.11.026.

Escobal, P. R. 1963. "Rise and set time of a satellite about an oblate planet." *AIAA J.* 1 (10): 2306–2310. https://doi.org/10.2514/3.2057.

European Space Agency. 2021. "Studies/reviews." Accessed November 3, 2021. https://www.esa.int/Enabling_Support/Space_Engineering_Technology/CDF/Studies_Reviews.

Fernández-Rico, G., I. Pérez-Grande, A. Sanz-Andres, I. Torralbo, and J. Woch. 2016. "Quasi-autonomous thermal model reduction for steady-state problems in space systems." *Appl. Therm. Eng.* 105 (Jul): 456–466. https://doi.org/10.1016/j.applthermaleng.2016.03.017.

Fortescue, P., G. Swinerd, and J. Stark. 2011. "Spacecraft system engineering." Chap. 20 in *Spacecraft systems engineering*. Hoboken, NY: Wiley.

Fu, W., J. Ma, P. Chen, and F. Chen. 2019. "Remote sensing satellites for digital earth." In *Manual of digital earth*, 55–123. Singapore: Springer.

García-Pérez, A. 2020. "Optimum preliminary design of ion thrusters in concurrent design facility." *Concurrent Eng.* 28 (3): 189–197. https://doi.org/10.1177/1063293X20938422.

García-Pérez, A., M. C. Manguán, Á. Sanz-Andrés, and G. Alonso. 2019a. "Numerical results of modal coupling in the UPMSat-2 structure." In *Proc., 8th European Conf. for Aeronautics and Space Sciences (EUCASS)*. Sint-Genesius-Rode: EUCASS.

García-Pérez, A., Á. Sanz-Andrés, G. Alonso, and M. C. Manguán. 2019b. "Dynamic coupling on the design of space structures." *Aerosp. Sci. Technol.* 84 (Jan): 1035–1048. https://doi.org/10.1016/j.ast.2018.11.045.

García-Pérez, A., F. Sorribes-Palmer, G. Alonso, and A. Ravanbakhsh. 2018. "Overview and application of FEM methods for shock analysis in space instruments." *Aerosp. Sci. Technol.* 80 (Sep): 572–586. https://doi.org/10.1016/j.ast.2018.07.035.

García-Pérez, A., F. Sorribes-Palmer, G. Alonso, and A. Ravanbakhsh. 2019c. "FEM simulation of space instruments subjected to shock tests by mechanical impact." *Int. J. Impact Eng.* 126 (Apr): 11–26. https://doi.org/10.1016/j.ijimpeng.2018.12.008.

Gómez-San-Juan, A., I. Pérez-Grande, and A. Sanz-Andrés. 2018. "Uncertainty calculation for spacecraft thermal models using a generalized sea method." *Acta Astronaut.* 151 (Oct): 691–702. https://doi.org/10.1016/j.actaastro.2018.05.045.

Gómez-San-Juan, A. M., J. C. Cano, and S. P. Carrion. 2020. "On the thermo-electric modelling of smallsats." In *Proc. 2020 Int. Conf. on Environmental Systems*. Emmaus, PA: ICES.

Han, C., S. Bai, S. Zhang, X. Wang, and X. Wang. 2019. "Visibility optimization of satellite constellations using a hybrid method." *Acta Astronaut.* 163 (Part B): 250–263. https://doi.org/10.1016/j.actaastro.2019.01.025.

Han, C., X. Gao, and X. Sun. 2017. "Rapid satellite-to-site visibility determination based on self-adaptive interpolation technique." *Sci. China Technol. Sci.* 60 (2): 264–270. https://doi.org/10.1007/s11431-016-0513-8.

Han, C., P. Yang, X. Wang, and S. Liu. 2018. "A fast computation method for the satellite-to-site visibility." In *Proc., 2018 IEEE Congress on Evolutionary Computation (CEC)*, 1–8. New York: IEEE.

Hihn, J., D. Chattopadhyay, G. Karpati, and M. McGuire. 2011. "Aerospace concurrent engineering design teams: Current state, next steps and a vision for the future." In *Proc., AIAA SPACE 2011 Conf. and Exposition*. Reston, VA: American Institute of Aeronautics and Astronautics.

IDR/UPM Institute (Instituto de Microgravedad "Ignacio Da Riva). 2020. "Mission requirements document (MRD)." Accessed November 3, 2021. https://martinlara3.webnode.es/martinlara-mission/.

Li, Y., S. Zhao, and J. Wu. 2016. "A general evaluation criterion for the coverage performance of LEO constellations." *Aerosp. Sci. Technol.* 48 (Jan): 94–101. https://doi.org/10.1016/j.ast.2015.11.003.

Liang, S., X. Li, and J. Wang. 2012. *Advanced remote sensing. A systematic view of remote sensing*. 1st ed. London: Academic.

Mai, Y., and P. Palmer. 2001. "Fast algorithm for prediction of satellite imaging and communication opportunities." *J. Guid. Control Dyn.* 24 (6): 1118–1124. https://doi.org/10.2514/2.4846.

McDonald, M., and V. Badescu. 2014. *The international handbook of space technology*. Berlin: Springer.

National Oceanic and Atmospheric Administration. 2016. "Wandering of the geomagnetic poles." Accessed November 3, 2021. https://www.ngdc.noaa.gov/geomag/GeomagneticPoles.shtml.

Nugnes, M., C. Colombo, and M. Tipaldi. 2019. "Coverage area determination for conical fields of view considering an oblate earth." *J. Guid. Control Dyn.* 42 (10): 2233–2245. https://doi.org/10.2514/1.G004156.

Palacios Lazaro, M. A., M. Bergadà Pujades, R. González Sola, A. Gamonal Coto, J. L. Garcia Fernández, and Y. Camacho. 2014. "Design, development and calibration of the MWR microwave radiometer on board Sentinel-3." In *European Microwave Week 2014: Connecting the Future, EuMW 2014—Conf. Proc., EuMC 2014: 44th European*

Microwave Conf., 1671–1674. Louvain-la-Neuve, Belgium: European Microwave Association.

Pindado, S., et al. 2016. "Master in space systems, an advanced master's degree in space engineering." In *Proc., ATINER's Conf. Paper Series ENGEDU2016-1953*, 1–16. Athens, Greece: Athens Institute for Education & Research.

Pindado, S., and J. Cubas. 2017. "Simple mathematical approach to solar cell/panel behavior based on datasheet information." *Renewable Energy* 103 (Apr): 729–738. https://doi.org/10.1016/j.renene.2016.11.007.

Pindado, S., J. Cubas, E. Roibás-Millán, F. Bugallo-Siegel, and F. Sorribes-Palmer. 2018a. "Assessment of explicit models for different photovoltaic technologies." *Energies* 11 (6): 1353. https://doi.org/10.3390/en11061353.

Pindado, S., J. Cubas, E. Roibás-Millán, and F. Sorribes-Palmer. 2018b. "Project-based learning applied to spacecraft power systems: A long-term engineering and educational program at UPM University." *CEAS Space J.* 10 (3): 307–323. https://doi.org/10.1007/s12567-018-0200-1.

Pindado, S., J. Cubas, and F. Sorribes-Palmer. 2015. "On the analytical approach to present engineering problems: Photovoltaic systems behavior, wind speed sensors performance, and high-speed train pressure wave effects in tunnels." *Math. Probl. Eng.* 2015: 1–17. https://doi.org/10.1155/2015/897357.

Porras-Hermoso, A., D. Alfonso-Corcuera, J. Piqueras, E. Roibás-Millán, J. Cubas, J. Pérez-Ávarez, and S. Pindado. 2021. "Design, ground testing and on-orbit performance of a sun sensor based on cots photodiodes for the UPMSat-2 satellite." *Sensors* 21 (14): 4905. https://doi.org/10.3390/s21144905.

Rodriguez-Rojo, E., J. Cubas, E. Roibás-Millán, and S. Pindado. 2019. "On the UPMSat-2 attitude, control and determination subsystems design." In *Proc., 8th European Conf. for Aeronautics and Space Sciences.* Rhode-St-Genese, Belgium: European Conference for AeroSpace Sciences.

Roibás-Millán, E., D. Alfonso-Corcuera, J. Cubas, J. M. Álvarez, S. Pindado, and A. M. Gomez-San-Juan. 2020a. "Performance analysis of photovoltaic systems: Research at IDR/UPM institute." In *Proc., 2020 IEEE International Conf. on Environment and Electrical Engineering and 2020 IEEE Industrial and Commercial Power Systems Europe (EEEIC/I CPS Europe)*, 1–6. New York: IEEE.

Roibás-Millán, E., A. Alonso-Moragón, A. G. Jiménez-Mateos, and S. Pindado. 2017. "Testing solar panels for small-size satellites: The UPMSat-2 mission." *Meas. Sci. Technol.* 28 (11): 115801. https://doi.org/10.1088/1361-6501/aa85fc.

Roibás-Millán, E., J. L. Cubero-Estalrrich, A. Gonzalez-Estrada, R. Jado-Puente, M. Sanabria-Pinzón, D. Alfonso-Corcuera, J. M. Álvarez, J. Cubas, and S. Pindado. 2020b. "Lambert w-function simplified expressions for photovoltaic current-voltage modelling." In *Proc., 2020 IEEE Int. Conf. on Environment and Electrical Engineering and 2020 IEEE Industrial and Commercial Power Systems Europe (EEEIC/I CPS Europe)*, 1–6. New York: IEEE.

Roibás-Millán, E., F. Sorribes-Palmer, and M. Chimeno-Manguán. 2018a. "The MEOW lunar project for education and science based on concurrent engineering approach." *Acta Astronaut.* 148 (Jul): 111–120. https://doi.org/10.1016/j.actaastro.2018.04.047.

Roibás-Millán, E., F. Sorribes-Palmer, J. Cubas, S. Pindado, M. Chimeno-Manguan, A. Gustavo, A. Sanz-Andres, J. Perez-Alvarez, S. Franchini, and I. Pérez-Grande. 2018b. "Implementation of concurrent engineering in muse (master in space systems) master's degree in space engineering." In *Proc., 3rd Annual Int. Conf. on Engineering Education & Teaching (ENGEDU—ATINER)*. Athens, Greece: Athens Institute for Education & Research.

Salvatore, A., J. Negron, and M. Jennifer. 1992. "Rapid determination of satellite visibility periods." *J. Astronaut. Sci.* 40: 17 40 (2): 281–296.

Sun, X., H. Cui, C. Han, and T. Geshi. 2012. "APCHI technique for rapidly and accurately predicting multi-restriction satellite visibility." In Vol. 143 of *Proc., 22nd AAS/AIAA Space Flight Mechanics Meeting*. Springfield, VA: American Astronautical Society.

Torralbo, I., I. Perez-Grande, A. Sanz-Andrés, and J. Piqueras. 2018. "Correlation of spacecraft thermal mathematical models to reference data." *Acta Astronaut.* 144 (Mar): 305–319. https://doi.org/10.1016/j.actaastro.2017.12.033.

Toth, C., and G. Jozkow. 2016. "Remote sensing platforms and sensors: A survey." *ISPRS J. Photogramm. Remote Sens.* 115 (May): 22–36. https://doi.org/10.1016/j.isprsjprs.2015.10.004.

Ulybyshev, Y. 2000. "Geometric analysis of low-earth-orbit satellite communication systems: Covering functions." *J. Spacecr. Rockets* 37 (3): 385–391. https://doi.org/10.2514/2.3572.

Vallado, D. A. 2013. Chap. 11 in *Fundamentals of astrodynamics and applications*. 4th ed. Cleveland: Microcosm Press.

Wang, X., C. Han, P. Yang, and X. Sun. 2019. "Onboard satellite visibility prediction using metamodeling based framework." *Aerosp. Sci. Technol.* 94 (Nov): 105377. https://doi.org/10.1016/j.ast.2019.105377.

Wertz, J. R., and W. Larson. 1999. Chap. 7 in *Space mission analysis and design*. 3rd ed. Cleveland: Microcosm Press.

Zhang, P., C. Xu, C. Hu, and Y. Chen. 2012. "Coordinate transformations in satellite navigation systems." In *Electrical Engineering, 140 LNEE*, 249–257. Berlin: Springer.

Zhou, Y., H. Leung, and M. Blanchette. 1996. "Sensor alignment using the earth-centered earth-fixed (ECEF) coordinate system." In Vol. 1 of *Proc., Conf. Record of the 30th Asilomar Conf. on Signals, Systems and Computers*, 469–473. Grove, CA: Asilomar.